PHYSICAL REVIEW B **98**, 144428 (2018)

Coexistence of magnetic fluctuations and long-range order in the one-dimensional J_1-J_2 zigzag chain materials $BaDy_2O_4$ and $BaHo_2O_4$

Bobby Prévost,[1] Nicolas Gauthier,[2] Vladimir Y. Pomjakushin,[3] Bernard Delley,[4] Helen C. Walker,[5]
Michel Kenzelmann,[2] and Andrea D. Bianchi[1,*]
[1] *Département de Physique & Regroupement Québécois sur les Matériaux de Pointe (RQMP),*
Université de Montréal, Montréal, Québec H3C 3J7, Canada
[2] *Laboratory for Scientific Developments and Novel Materials, Paul Scherrer Institut, CH-5232 Villigen PSI, Switzerland*
[3] *Laboratory for Neutron Scattering, Paul Scherrer Institute, CH-5232 Villigen, Switzerland*
[4] *Condensed Matter Theory Group, Paul Scherrer Institut, CH-5232 Villigen PSI, Switzerland*
[5] *ISIS Facility, STFC Rutherford Appleton Laboratory, Chilton, Didcot, Oxfordshire OX11 0QX, United Kingdom*

(Received 11 May 2018; revised manuscript received 3 September 2018; published 19 October 2018)

The compounds $BaDy_2O_4$ and $BaHo_2O_4$ are part of a family of frustrated systems exhibiting interesting properties, including spin-liquid-type ground states, magnetic-field-induced phases, and the coexistence of short- and long-range magnetic order, with dominant one-dimensional correlations, which can be described as Ising J_1-J_2 zigzag chains along the c axis. We have investigated polycrystalline samples of $BaDy_2O_4$ and $BaHo_2O_4$ with both neutron diffraction and neutron spectroscopy, coupled to detailed crystalline electric field calculations. The latter points to site-dependent anisotropic magnetism in both materials, which is corroborated by the magnetic structures we determined. The two systems show the coexistence of two different long-range orders: two double Néel $\uparrow\uparrow\downarrow\downarrow$ orders in the ab plane with propagation vectors $\mathbf{k}_1 = (\frac{1}{2}, 0, \frac{1}{2})$ and $\mathbf{k}_2 = (\frac{1}{2}, \frac{1}{2}, \frac{1}{2})$ for $BaDy_2O_4$, and two distinct arrangements of simple Néel $\uparrow\downarrow\uparrow\downarrow$ orders along the c axis, both with the propagation vector $\mathbf{k}_0 = (0, 0, 0)$ for $BaHo_2O_4$. The order for both wave vectors in $BaDy_2O_4$ occurs at $T_N = 0.48$ K, while in $BaHo_2O_4$ the first order sets in at $T_N \sim 1.3$ K and the second one has a lower ordering temperature of 0.84 K. Both compounds show extensive diffuse scattering which we successfully modeled with a one-dimensional axial next-nearest neighbor Ising (ANNNI) model. In both materials, strong diffusive scattering persists to temperatures well below where the magnetic order is fully saturated.

DOI: 10.1103/PhysRevB.98.144428

I. INTRODUCTION

Among the pyrochlores, spinels, and kagome structures, a newly synthesized family of magnetically frustrated compounds with general formula $AkLn_2O_4$ (where Ak = alkaline earth metal, and Ln = lanthanide) has recently attracted attention [1], as they offer a novel route to magnetic frustration. This family of compounds shows a large variety of magnetic properties, ranging from the coexistence of short- and long-range magnetic order [2–7] to the complete absence of magnetic order down to the lowest accessible temperature despite strong magnetic interactions [8–10]. In applied fields, the magnetization shows the formation of plateaus at 1/3 of the saturation value [11], which are concurrent with field-induced magnetic order [12–16].

The crystalline structure of the $AkLn_2O_4$ compounds, shown in Fig. 1, belongs to the *Pnam* space group, where the lattice of magnetic rare earth ions forms hexagonal tiles in the ab plane and zigzag chains along the c axis. In this structure, each rare earth ion is located inside a differently distorted O octahedron, resulting in two inequivalent rare earth sites with a distinct crystal electric field (CEF) environment. It has been argued that the unusual magnetism in $SrLn_2O_4$ originates from the chains, which can be described as an effective one-dimensional (1D) Ising J_1-J_2 spin chain model [7,17], commonly referred as the 1D axial next-nearest neighbor Ising (ANNNI) model [18]. The spin anisotropy in $AkLn_2O_4$ is controlled by the CEF, which splits the J multiplet of the rare earth ions [8]. The observed CEF splitting results in an Ising-type interaction between the rare earth moments, reducing the effective dimension of the exchange to a zigzag chain of spins.

Antiferromagnetic zigzag chains, such as $AkLn_2O_4$, combine the effect of low dimensionality with magnetic frustration due to the antiferromagnetic next-nearest neighbor interactions. In applied magnetic fields, zigzag chains show a plateau in the magnetization at 1/3 of the saturation value, even in the classical limit [19], and a rich magnetic phase diagram [20]. Also, while conventional long-range order is prohibited by the Mermin-Wagner theorem, zigzag chains can still acquire chiral order, which should survive to finite temperatures [21]. In a chirally ordered state, spins have a tendency to "rotate" in a preferred plane with a preferred rotational direction [21].

In the ANNNI model, the ground state at zero temperature is determined through competing interactions between the nearest neighbors J_1 and the next-nearest neighbors J_2:

$$\mathcal{H} = \sum_i J_1 \hat{S}_i^z \hat{S}_{i+1}^z + J_2 \hat{S}_i^z \hat{S}_{i+2}^z. \tag{1}$$

---

[*] Corresponding address: andrea.bianchi@umontreal.ca

2469-9950/2018/98(14)/144428(12)

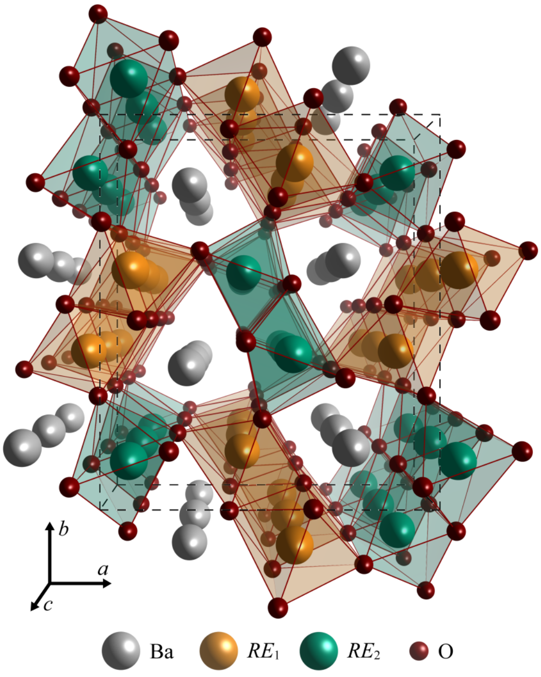

FIG. 1. Crystal structure of $AkLn_2O_4$, where Ak = alkaline earth metal and Ln = lanthanide, viewed along the *c* direction. This structure contains two inequivalent rare earth sites which form to a good approximation magnetically independent zigzag chains along the *c* axis. The unit cell is shown as the dotted box containing four chains.

The ANNNI model can accommodate different types of antiferromagnetic order, depending on the ratio J_2/J_1 of the interactions [22]. The ground state is a simple Néel state for an antiferromagnetic J_1 and a J_2 which is either ferromagnetic or weakly antiferromagnetic, such that $J_2 > -0.5|J_1|$. A double Néel state forms for an antiferromagnetic J_2 with $J_2 < -0.5|J_1|$, where J_1 can be either ferromagnetic, or antiferromagnetic. A ratio close to the critical value separating these two ground states leads to strong fluctuations, which is a source of frustration.

In this paper, we present a detailed investigation of the magnetic structure of $BaDy_2O_4$ and $BaHo_2O_4$ for which only growth, specific heat, and magnetization have been reported [23,24]. The motivation behind this investigation is a direct comparison with the isotructural compounds $Sr(Dy, Ho)_2O_4$ by replacing the noninteracting Sr atoms with larger Ba atoms. As the interactions are governed by crystalline electric field effects, which are very sensitive to local structure, the change from Sr to Ba will change the anisotropy and strength of the magnetic interactions.

II. RESULTS AND ANALYSIS

A. Samples preparation and experimental technique

$BaDy_2O_4$ and $BaHo_2O_4$ powders were prepared by solid state reaction using high purity starting materials. Stoichiometric mixtures of Dy_2O_3/Ho_2O_3 (99.995%) and $BaCO_3$ (99.994%), with a 1% surplus of carbonate, both dried at 600 °C and weighed in a glove box, were mixed in a ball mill and pressed into a rod. The rods were heated in an argon atmosphere at 1300 °C in an alumina crucible for 12 hours. The solidified rods were ground, repressed into rods, and heated once more under the same condition. This resulted in single-phase samples, as determined by x-ray powder diffraction. For specific heat measurements, small single crystals of $BaHo_2O_4$ were grown from Ba flux following the method described by Besara *et al.* [24].

In order to establish the CEF splitting of the ground state multiplets $J = 15/2$ and $J = 8$ of the Dy^{3+} and the Ho^{3+} ions, respectively, inelastic neutron scattering experiments were performed on powders of both $BaDy_2O_4$ and $BaHo_2O_4$ using the MERLIN time-of-flight spectrometer at ISIS in the United Kingdom [25]. The two samples were mounted in a double-walled aluminum cylinder to maximize the scattering intensities [26]. Spectra were acquired for both samples at incident neutron energies E_i of 12.30, 20.00, 38.20, and 100.00 meV and temperatures T of 7, 75, and 150 K. Calculations of the CEF energy levels and the inelastic neutron spectra were performed with the program MULTIX [27].

To determine the magnetic structure of the compounds, elastic neutron scattering data were acquired on the same powders using the HRPT diffractometer at the Paul Scherrer Institut (PSI) in Switzerland [28]. Data were collected from $T = 0.07$ K up to 30 K at a neutron wavelength λ of 1.886 Å for $BaDy_2O_4$, and from $T = 0.20$ up to 60 K at the same wavelength, with additional data at $\lambda = 1.155$ Å for $BaHo_2O_4$. Due to the strong neutron absorption of Dy, the $BaDy_2O_4$ powder was loaded into a double walled copper cylinder, while for $BaHo_2O_4$ a simple copper cylinder was used. The magnetic structure was refined through a Rietveld analysis with the FULLPROF Suite [29].

Magnetization measurements on the powders were carried out using a Quantum Design superconducting quantum interference device with a vibrating sample magnetometer (SQUID-VSM), equipped with a 7 T magnet, over the temperature range from 300 K down to 1.8 K. The specific heat measurements were made using a Quantum Design physical property measurement system (PPMS) equipped with a ^{3}He refrigerator, down to a temperature of 0.35 K.

B. Crystalline electric fields excitations

The motivation for carrying out the inelastic neutron scattering experiment backed up by CEF calculations was to establish a basis for the characterization of the magnetic structures in the following sections. The results from the CEF model for the magnetic anisotropy and direction of the easy axis are important for developing a magnetic model.

The calculations of the CEF levels rely on a detailed crystallographic structure as input. For this we refined the structure from the diffraction data at high angles 2θ, as the magnetic scattering intensity dominates at low angles. For $BaHo_2O_4$, a simultaneous refinement of the data acquired at wavelengths λ of 1.886 and 1.155 Å was performed. We found only a small variations of the O distances over the entire range of temperatures from 60 K down to 0.07 K, as shown in Fig. 2. The chemical unit cell volume varies by about 0.5 Å^3 for $BaDy_2O_4$, and there is no volume change for $BaHo_2O_4$ within the experimental accuracy. The slight change in the

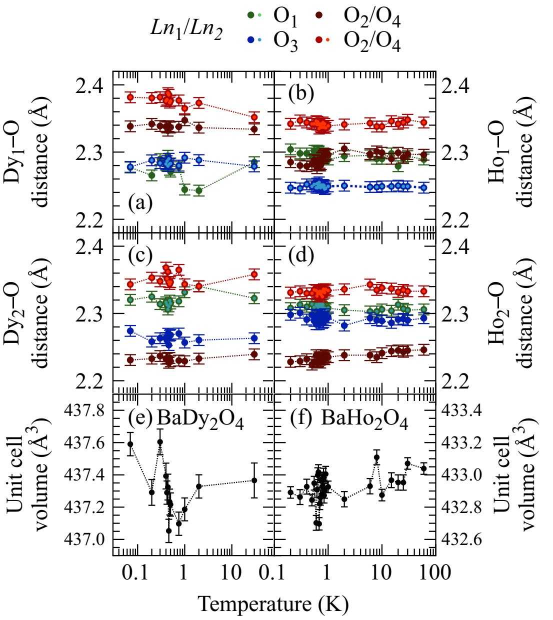

FIG. 2. Temperature dependence of the crystal structure from a refinement of the elastic neutron scattering data. Panels (a)–(d) show the distance between the rare earth atoms and the six surrounding O atoms, which is constant within the resolution of our experiment. The labels on the O atoms represent their four different positions in this crystal structure. Panels (e) and (f) present the very small variation of the unit cell volume.

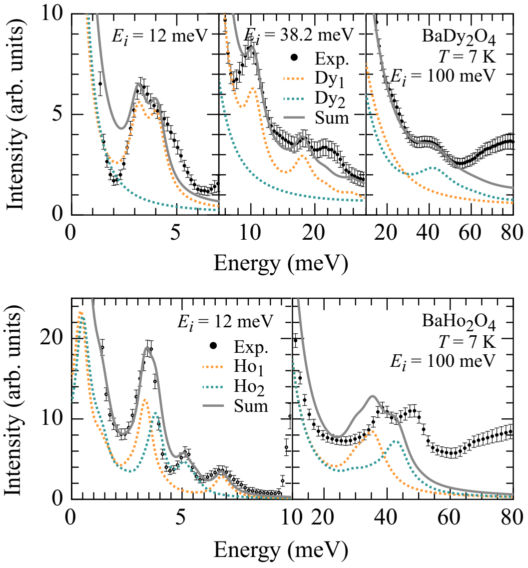

FIG. 3. Inelastic neutron scattering spectra for $BaDy_2O_4$ (top) and $BaHo_2O_4$ (bottom) at $T = 7$ K for various incident energies E_i. The solid line is the sum of the contributions from the two rare earth sites. The contribution from site 1 is shown as the orange dashed line and the contribution from site 2 is shown as the blue dashed line. The lines were obtained by fitting the experimental spectra with calculations using the program MULTIX.

lattice parameters of $BaDy_2O_4$ is accompanied by a small increase of the Bragg peaks' width. The intra-chain distance between the rare earth atoms is also temperature independent and not affected by the magnetic order, as are the dimensions of the O octahedra surrounding the magnetic ions. For $BaDy_2O_4$, the lattice parameters are $a = 10.4068(3)$ Å, $b = 12.1131(3)$ Å, and $c = 3.46985(10)$ Å at $T = 0.07$ K, and, for $BaHo_2O_4$, $a = 10.3864(3)$ Å, $b = 12.0852(2)$ Å, and $c = 3.44754(8)$ Å at $T = 0.20$ K. These values are similar to those reported by Doi *et al.* [23].

The program MULTIX was used to calculate the inelastic neutron spectra for comparison with the experimental spectra. It computes the energy levels of an individual magnetic ion in the CEF defined by the charges at the positions of the neighboring ions. This permits the characterization of the single-ion anisotropy. Here, we are taking advantage of the fact that MULTIX allows us to calculate CEF levels in systems with low symmetry, such as the $BaLn_2O_4$ structure, where the only point symmetry at the rare earth site is a mirror plane.

The CEF energy levels are calculated in MULTIX by taking into account the Coulomb and spin-orbit interaction, as well as an overall CEF scaling factor, which scales the effective charge on the ions. Since we found the computed spectra fairly insensitive to the scaling of the strength of the Coulomb and spin-orbit interaction, only the CEF scaling factor S_{xtal} was refined. This results in a fair agreement with the experimental spectra, as shown in Fig. 3. The calculations were carried out independently for the two crystallographically inequivalent rare earth sites, with a different CEF scaling factor for each site. In order to compare the calculations with the inelastic neutron spectra, the contribution from both sites was added. For $BaDy_2O_4$ the best fit was obtained with $S_{\mathrm{xtal}}^{\mathrm{Dy}_1} = 0.19$ and $S_{\mathrm{xtal}}^{\mathrm{Dy}_2} = 0.64$, and for $BaHo_2O_4$ it was obtained with $S_{\mathrm{xtal}}^{\mathrm{Ho}_1} = 0.45$ and $S_{\mathrm{xtal}}^{\mathrm{Ho}_2} = 0.58$. These low values of the S_{xtal} parameters are similar to what has been observed in $Sr(Dy, Ho)_2O_4$ [8], originating from the contraction of the f orbital or an overestimation of the ionic charges. An additional parameter was added to model the experimental broadening of the spectra. In the case of $BaDy_2O_4$, the level of the first excited state is found at $E = 2.6$ and 42.9 meV for the Dy_1^{3+} and Dy_2^{3+} sites, respectively, while for $BaHo_2O_4$ these levels are much closer to the ground states, with $E = 0.2$ and 0.3 meV for Ho_1^{3+} and Ho_2^{3+}, respectively. A comparison between the energy levels obtained by fitting the inelastic neutron scattering spectra and the position of the peaks in the spectra is shown in Fig. 4. Here, the positions of the experimental levels were determined by fitting Gaussian functions to the peaks in the spectra.

The MULTIX calculations also predict the size and direction of the magnetic moments. Each Dy^{3+} ion has a doublet ground state protected by time reversal symmetry due to the fact that Dy^{3+} is a Kramers ion. For each Ho^{3+}, which is a non-Kramers ion, the ground state is treated as a pseudodoublet because the lowest energy states are two singlets separated by an energy difference smaller than the computational accuracy. The moments obtained by this procedure are listed in Table I. For $BaDy_2O_4$, the moments for both sites lie in the *ab* plane, with one predominantly along the *a* axis and the other along the *b* axis. For $BaHo_2O_4$, the first site has a moment in the *ab* plane, while for the second site the moment is along the *c* axis. There is a clear distinction between moments

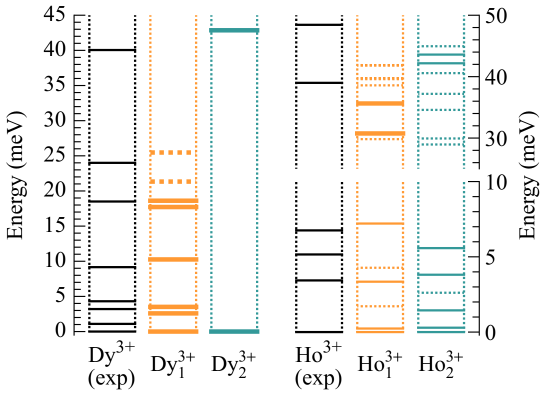

FIG. 4. The CEF level scheme of $BaDy_2O_4$ (left) and $BaHo_2O_4$ (right) as established by fitting the levels from MULTIX to the inelastic neutron scattering spectra measured at $T = 7$ K. The thick lines in the theoretical levels represent doublet or clear pseudodoublet states, regular lines are singlet states, and dashed lines indicate levels of significantly lower intensity, which makes them hard to see in Fig. 3. For a comparison with the calculations, Gaussian peaks were fitted to the visible peaks of the inelastic neutron scattering spectra, where the center of each Gaussian is shown as a line.

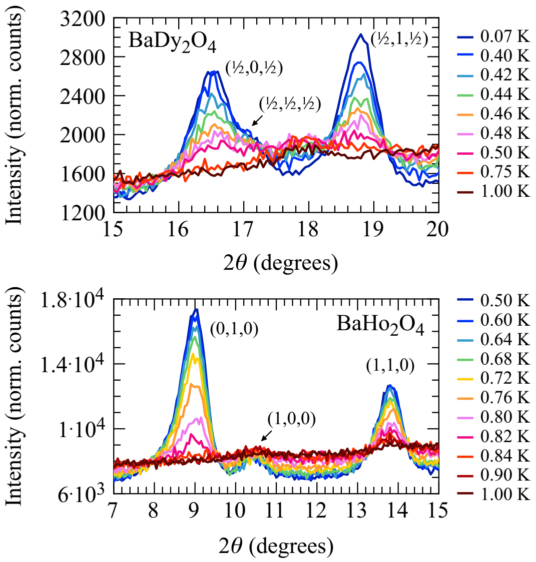

FIG. 5. Thermal evolution of the magnetic Bragg peaks at low diffraction angles. The top panel shows the magnetic peaks of $BaDy_2O_4$ at $\mathbf{Q}$ of $(\frac{1}{2}, 0, \frac{1}{2})$, $(\frac{1}{2}, \frac{1}{2}, \frac{1}{2})$, and $(\frac{1}{2}, 1, \frac{1}{2})$, indicating the presence of two propagation vectors, $\mathbf{k}_1 = (\frac{1}{2}, 0, \frac{1}{2})$ and $\mathbf{k}_2 = (\frac{1}{2}, \frac{1}{2}, \frac{1}{2})$. The data for $BaHo_2O_4$ are shown on the lower panel, were magnetic peaks appear at $\mathbf{k} = (0, 0, 0)$ values of $\mathbf{Q}$.

laying exclusively in the *ab* plane or exclusively along the *c* axis: perpendicular or along the chains. This points to a clear anisotropy of the magnetic interactions, as previously observed for the Sr variant of these compounds. We observe the following total moments per each site: $|\boldsymbol{\mu}_{\mathrm{Dy}_1}| = 9.7\mu_B$, $|\boldsymbol{\mu}_{\mathrm{Dy}_2}| = 9.8\mu_B$, $|\boldsymbol{\mu}_{\mathrm{Ho}_1}| = 9.7\mu_B$, and $|\boldsymbol{\mu}_{\mathrm{Ho}_2}| = 7.9\mu_B$. Of these, only the second Ho site has a moment which is significantly lower than the effective moment expected from Hund's rules: $10.4\mu_B$ for both Dy^{3+} and Ho^{3+} ions [30]. Fitting a Curie-Weiss model to the magnetic susceptibilities at high temperatures results in an effective moment μ_{eff} per magnetic site of $10.60(1)\mu_B$ and $10.77(1)\mu_B$ for $BaDy_2O_4$ and $BaHo_2O_4$, respectively, with Curie-Weiss temperatures θ_{CW} of $-18.5(3)$ and $-10.9(3)$ K.

The CEF level scheme of $BaDy_2O_4$ was robust to repositioning the atoms within the error bars of our structural refinement, and only a scaling of the level separation was observed. However, in $BaHo_2O_4$, the level scheme was more strongly affected, and significantly changes when the O positions are set to the limit of the uncertainties of our refinement. Despite the absence of clear structural changes, the MULTIX calculations would nonetheless benefit from higher resolution data from an x-ray synchrotron source to observe potential distortion of the O octahedra. Additional measurements are planned, such as electron paramagnetic resonance (EPR) and photoluminescence spectroscopy, as were used in the case of $SrEr_2O_4$ to determine the CEF levels [31].

TABLE I. Direction and size in μ_B of the magnetic moments as determined from crystal field calculations (CEF), using MULTIX, and from a refinement of the magnetic Bragg peaks of elastic neutron scattering (exp), for the two inequivalent rare earth sites in the $AkLn_2O_4$ structure.

	μ_a	μ_b	μ_c	$\lvert\boldsymbol{\mu}\rvert$		μ_a	μ_b	μ_c	$\lvert\boldsymbol{\mu}\rvert$
$Dy_{1_{\mathrm{CEF}}}$	9.4	2.4	0.1	9.7	$Dy_{1_{\mathrm{exp}}}$	2.9	4.2	0.0	5.1
$Dy_{2_{\mathrm{CEF}}}$	1.9	9.6	0.0	9.8	$Dy_{2_{\mathrm{exp}}}$	0.0	2.3	0.0	2.3
$Ho_{1_{\mathrm{CEF}}}$	1.2	9.6	0.0	9.7	$Ho_{1_{\mathrm{exp}}}$	Not ordered			
$Ho_{2_{\mathrm{CEF}}}$	0.0	0.0	7.9	7.9	$Ho_{2_{\mathrm{exp}}}$	0.0	0.0	6.2	6.2

C. Magnetic structure

1. $BaDy_2O_4$

Information related to the ordering temperature as well as the nature of the magnetic order can be deduced from the temperature dependence of the powder diffraction spectra. Spectra at low diffraction angles 2θ from base temperature to $T = 1$ K are shown in Fig. 5. In the case of $BaDy_2O_4$, upon cooling below $T = 0.48$ K, additional Bragg peaks appear at 2θ values of 16.5°, 17.1°, and 18.8°. These peaks can be indexed with a momentum transfer $\mathbf{Q}$ of $(\frac{1}{2}, 0, \frac{1}{2})$, $(\frac{1}{2}, \frac{1}{2}, \frac{1}{2})$, and $(\frac{1}{2}, 1, \frac{1}{2})$, which indicate a magnetic order with two propagation vectors $\mathbf{k}_1 = (\frac{1}{2}, 0, \frac{1}{2})$ and $\mathbf{k}_2 = (\frac{1}{2}, \frac{1}{2}, \frac{1}{2})$.

On a wider range of angles, as shown in Figs. 6(a)–6(b), one can notice the evolution of an additional magnetic scattering signal when the magnetic transition temperature is approached. This additional signal has the form of a sawtooth, which is reminiscent of the powder average from one- or two-dimensional magnetic correlations [32,33]. This diffuse scattering is present in both compounds, and, contrary to what one would expect for a fully ordered system, it does not completely disappear with the onset of the magnetic Bragg peaks, but remains visible down to the lowest measured temperatures. The main feature of the diffuse scattering is located between the Bragg peaks at $\mathbf{Q} = (\frac{1}{2}, \frac{1}{2}, \frac{1}{2})$ and $(\frac{1}{2}, 1, \frac{1}{2})$, at $2\theta \sim 18°$. It is outlined by the strong scattering intensity in the color plot and clearly visible up to at least $T = 2$ K. Below

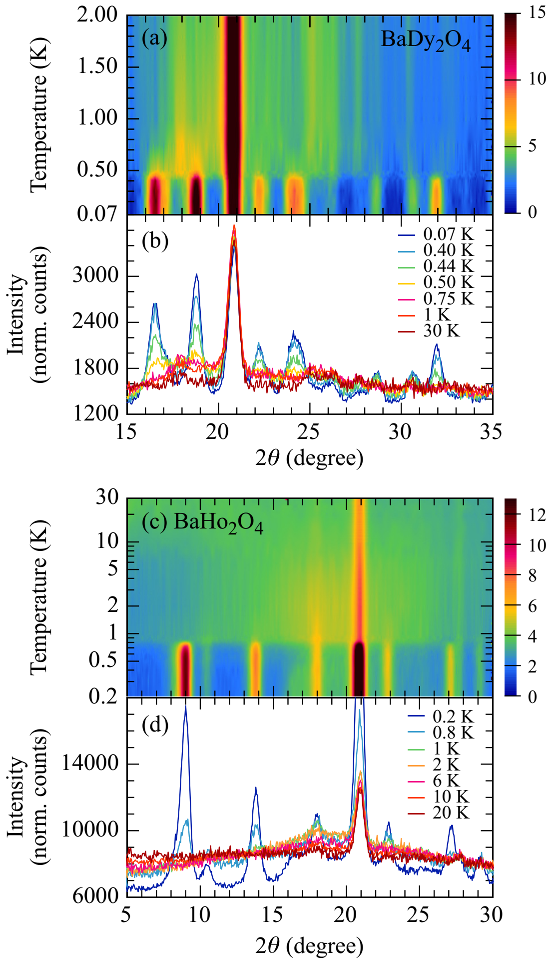

FIG. 6. Region showing the principal magnetic Bragg peaks to illustrate the thermal evolution of the diffuse scattering. The diffusive scattering is clearly visible in the two-dimensional color plots. Panels (a) and (b) show a sawtooth feature for BaDy$_2$O$_4$, which is centered at $2\theta \sim 18^\circ$ just above the transition. Panels (c) and (d) present a similar feature for BaHo$_2$O$_4$, also centered at $2\theta \sim 18^\circ$, which persists to temperatures below the ordering temperature of 0.84 K.

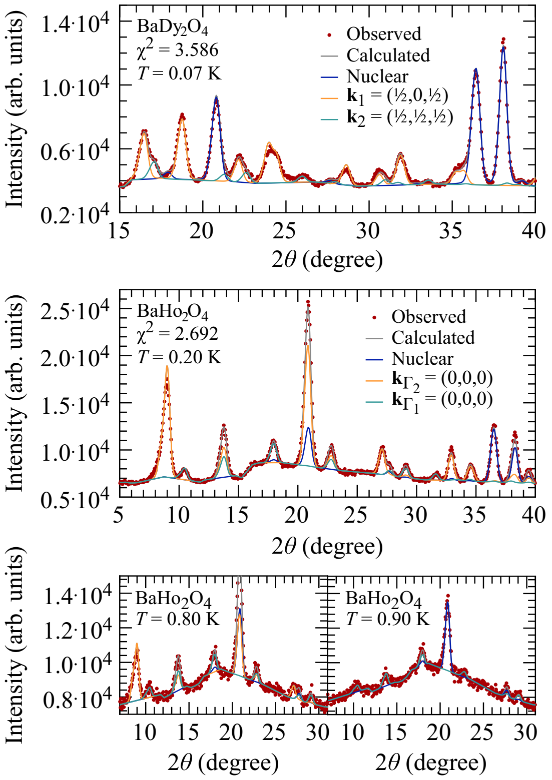

FIG. 7. FULLPROF refinement of the neutron diffraction patterns of BaDy$_2$O$_4$ (top) and BaHo$_2$O$_4$ (bottom) taken at $T = 0.07$ and 0.20 K, respectively. The nuclear and the different magnetic contributions are plotted separately. In BaDy$_2$O$_4$, the magnetic contributions come from two wave vectors, $\mathbf{k}_1 = (\frac{1}{2}, 0, \frac{1}{2})$ and $\mathbf{k}_2 = (\frac{1}{2}, \frac{1}{2}, \frac{1}{2})$. In BaHo$_2O_4$, the magnetic contributions have a single wave vector, $\mathbf{k}_0 = (0, 0, 0)$, but two different irreducible representations, Γ_1 and Γ_2. This results in two magnetic transitions with different critical temperatures. The lowest panel shows the refinement of the BaHo$_2$O$_4$ data close to the lower transition, where a new set of Bragg peaks emerges as the temperature is lowered from 0.9 to 0.8 K.

the transition, this feature is harder to see due to high density of magnetic Bragg peaks, but it persists down to the lowest measured temperatures. The color plot ends at $T = 2$ K, as the next pattern at a higher temperature was only taken at 30 K.

The result of the refinement of the BaDy$_2$O$_4$ diffraction pattern is shown in the top panel of Fig. 7. The natural solution for this magnetic order is that the two different ordering vectors are each associated with a crystallographically different rare earth site. The sharpness of the magnetic Bragg peaks indicates that the order is long range, as their widths are comparable to the nuclear Bragg peaks, which are resolution limited. However, a single-crystal experiment is required to precisely determine the correlation length. A visualization of the structures is given in Fig. 8.

Each of the two magnetic sites forms a chain which has a double Néel structure with a ↑↑↓↓ motif. As noted in Fig. 5, site 1 has a propagation vector $\mathbf{k}_1 = (\frac{1}{2}, 0, \frac{1}{2})$ and site 2 has $\mathbf{k}_2 = (\frac{1}{2}, \frac{1}{2}, \frac{1}{2})$, quadrupling and octupling the volume of the chemical unit cell. Both ordering vectors correspond to the same Shubnikov group with different irreducible representations (irreps) of the space group *Pnam*, as listed in Table II. Chain A has a ↑↑↓↓ motif for both sites. In contrast, on chain B, one site has a ↑↑↓↓ motif, the other a ↓↑↑↓ motif.

The structure was refined for all measured temperatures. As the intensity of the different magnetic peaks is proportional to the square of the magnetic moment associated with the magnetic order, it is possible to extract the temperature dependence of the size and direction of the moments. The results for both propagation vectors and irreps are shown in Fig. 9.

The refinement results in both moments lying in the *ab* plane: $\boldsymbol{\mu}_{\mathbf{k}_1} = (2.9, 4.2, 0.0)\mu_\mathrm{B}$ and $\boldsymbol{\mu}_{\mathbf{k}_2} = (0.0, 2.3, 0.0)\mu_\mathrm{B}$. Also, both moments order simultaneously at $T_\mathrm{N} = 0.48$ K, within the temperature resolution of our experiment, and they saturate already at 0.30 K.

From the analysis of the powder spectra, it is not possible to assign the different wave vectors to a particular rare earth site; the χ^2 from the refinements are not significantly different when we exchange the sites, or if both wave vectors are confined to a single site. Nonetheless, identification of the

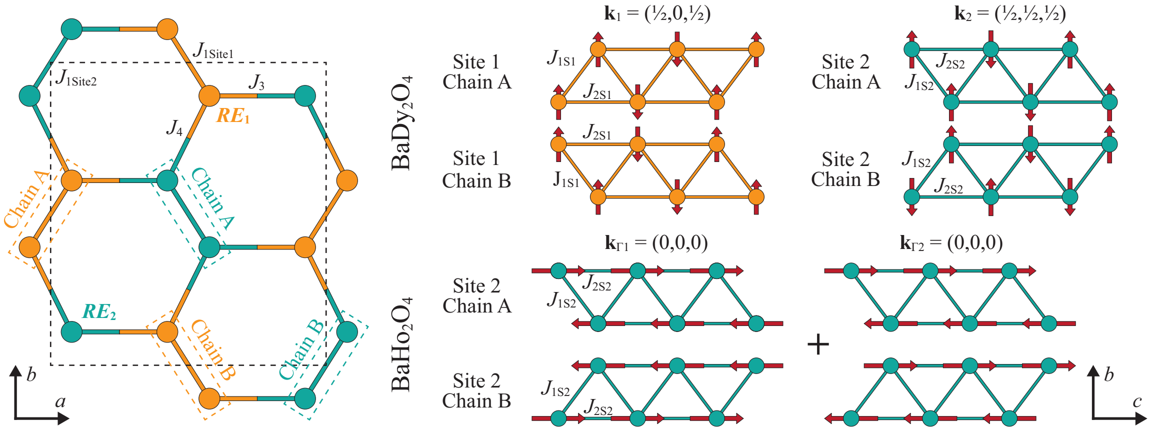

FIG. 8. Arrangement of the rare earth atoms and magnetic structure of BaDy$_2$O$_4$ and BaHo$_2$O$_4$. The left side illustrates a view of the *ab* plane, exhibiting the honeycomb pattern of the rare earth atoms, where the dotted box is a chemical unit cell. For a clearer view, Ba and O atoms were omitted, and the crystallographically nonequivalent rare earth sites, which each consist of two chains stretching along the *c* axis, are shown in a different color. J_1 and J_2 are the interaction constants for the nearest and next-nearest neighbors along the chains, while J_3 and J_4 are the interaction constants between nearest neighbors outside the chains, located in direction of *a* and *b*, respectively. On the right side of the figure, the chains along the *c* axis are isolated and projected onto the *bc* plane. In BaDy$_2$O$_4$, both ordering vectors represent a double Néel arrangement. For $\mathbf{k}_1$, the two chains A and B stay equivalent. However, for $\mathbf{k}_2$, the moments on chain B are shifted by one position with respect to their positions on chain A. Only a single transition temperature is observed, for both wave vectors. In BaHo$_2$O$_4$, site 2 exhibits a simple Néel order, which is split into two different irreps. Each irrep has its own ordering temperature, while the moments on site 1 do not order.

sites is possible by comparing the direction of the magnetic moments obtained from the CEF calculations for the different crystallographic sites, listed in Table I, with the direction of the moments from the refinement of the powder spectra. For BaDy$_2$O$_4$, the MULTIX calculations and the refinement from the experimental diffraction pattern both show that both moments are restricted to the *ab* plane. We can now use the relative strength of the components along *a* and *b* to distinguish between the two sites: the moment $\boldsymbol{\mu}_{\text{Dy}_1}$ is stronger along *a* and the moment $\boldsymbol{\mu}_{\text{Dy}_2}$ stronger along *b*. The resulting magnetic structure is shown in Fig. 8, where we show the different sites and chains separately for clarity. The discrepancies between the size of the magnetic moments from the refinements and those predicted by the CEF calculations can be explained by the presence of diffuse scattering, analyzed in Sec. II D.

2. BaHo$_2$O$_4$

For BaHo$_2$O$_4$, new peaks are observed for temperatures below $T = 0.84$ K at values of $\mathbf{Q}$ corresponding to a propagation vector $\mathbf{k}_0 = (0, 0, 0)$. They are clearly visible at low angles in Fig. 5. Additional intensity also appears at the position of nuclear Bragg peaks at higher diffraction angles.

The diffusive scattering in Figs. 6(c)–6(d) is similar to the case of BaDy$_2$O$_4$. However, it is easier to see in BaHo$_2$O$_4$ with its $\mathbf{k}_0$ propagation vector, where once again the diffusive signal is strongest at $2\theta \sim 18^\circ$. This diffuse scattering signal is still visible on the otherwise stable background up to $T = 30$ K, but also persists below the magnetic transition down to 0.20 K, where the feature becomes much sharper.

The result of the refinement of the diffraction patterns is shown in the lower panels of Fig. 7. Like its sister compound BaDy$_2$O$_4$, BaHo$_2$O$_4$ possesses two distinct magnetic orders, characterized by sharp resolution limited magnetic Bragg peaks. In this case, they consist of simple Néel chains ↑↓↑↓ with a propagation vector $\mathbf{k}_0 = (0, 0, 0)$, which does not increase the size of the unit cell. Two magnetic orders with different irreps, Γ_1 and Γ_2, are nonetheless needed in order to adequately account for magnetic scattering intensities. With such a propagation vector, each possible irrep is forced by

TABLE II. Irreducible representations of the space group *Pnam* for each propagation vector $\mathbf{k}$ of the magnetic structures of BaDy$_2$O$_4$ and BaHo$_2$O$_4$.

BaDy$_2$O$_4$	$\mathbf{k}_1 = (\frac{1}{2}, 0, \frac{1}{2})$	$\mathbf{k}_2 = (\frac{1}{2}, \frac{1}{2}, \frac{1}{2})$
x, y, z	$(C_1 - iC_4, C_2 - iC_5, C_3 + iC_6)$	$(C_1 - iC_4, C_2 - iC_5, C_3 + iC_6)$
$-x, -y, z + \frac{1}{2}$	$(-C_4 + iC_1, -C_5 + iC_2, -C_6 - iC_3)$	$(-C_4 + iC_1, -C_5 + iC_2, -C_6 - iC_3)$
$x + \frac{1}{2}, -y + \frac{1}{2}, -z + \frac{1}{2}$	$(-C_4 - iC_1, C_5 + iC_2, -C_6 + iC_3)$	$(C_4 + iC_1, -C_5 - iC_2, -C_6 + iC_3)$
$-x + \frac{1}{2}, y + \frac{1}{2}, -z$	$(C_1 + iC_4, -C_2 - iC_5, C_3 - iC_6)$	$(C_1 + iC_4, -C_2 - iC_5, -C_3 + iC_6)$
BaHo$_2$O$_4$	$\mathbf{k}_{\Gamma_1} = (0, 0, 0)$	$\mathbf{k}_{\Gamma_2} = (0, 0, 0)$
x, y, z	$(0, 0, C_1)$	$(0, 0, C_1)$
$-x, -y, z + \frac{1}{2}$	$(0, 0, -C_1)$	$(0, 0, -C_1)$
$x + \frac{1}{2}, -y + \frac{1}{2}, -z + \frac{1}{2}$	$(0, 0, C_1)$	$(0, 0, -C_1)$
$-x + \frac{1}{2}, y + \frac{1}{2}, -z$	$(0, 0, -C_1)$	$(0, 0, C_1)$

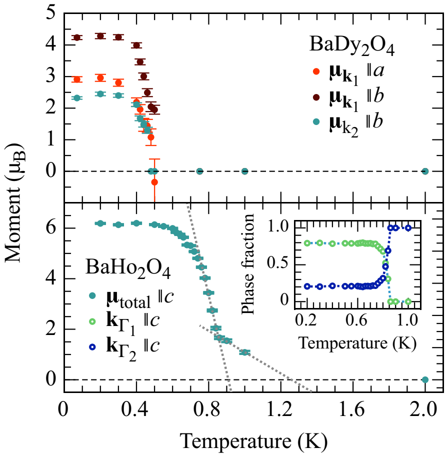

FIG. 9. Size and direction of the magnetic moment as determined from the refinement of the neutron powder diffraction data. In BaDy$_2$O$_4$, the moments for both wave vectors $\mathbf{k}_1$ and $\mathbf{k}_2$ order simultaneously at $T_N = 0.48$ K. In BaHo$_2$O$_4$, the two irreps, which have the same wave vector $\mathbf{k}_0 = (0, 0, 0)$, order at different temperatures. The dotted lines are linear extrapolations. The inset shows the phase fraction of the two irreps, where Γ_2 orders at approximately $T_{N\Gamma_2} \sim 1.3$ K and Γ_1 at $T_{N\Gamma_1} = 0.84$ K. At the lowest temperatures, the ratio between the two irreps stabilizes at 80%–20%.

symmetry to either carry a moment in the *ab* plane or along the *c* axis, whereas the irreps of $\mathbf{k}_1$ and $\mathbf{k}_2$ of BaDy$_2$O$_4$ are not restraining the moment direction.

Moreover, a close inspection of the data together with the refinement, presented in the lower panels of Fig. 7, show that the two orders—or sets of Bragg peaks—appear in two steps. The contribution from Γ_1 indicates order at 0.84 K, and the one from Γ_2 orders between 1 and 2 K, a temperature range in which unfortunately no additional data were gathered. Both orders share the same propagation vector and have ordered moments perpendicular to the *ab* plane, pointing along *c*. Interestingly, this points to a coexistence of the ordered moments on site 2, leaving the moment on site 1 disordered. This is then consistent with the MULTIX calculations which show that the moment of the Ho on site 2, $\boldsymbol{\mu}_{\text{Ho}_2}$, points along *c* while the moment on site 1, $\boldsymbol{\mu}_{\text{Ho}_1}$, is restricted to the *ab* plane. There are several possibilities to interpret this structure from the powder diffraction refinement. One rather unusual interpretation is to treat the two orders as distinct phases. This would imply the superposition of the two orders on the same site, resulting in magnetic moments on chains A and B with starkly different sizes.

The more physical scenario is that the correlations in the chains nucleate either one of the two magnetic structures, leading to a phase separation within a single chain. In this case, the same moment is placed on both irreps, while the phase fraction is allowed to vary. The refinement of BaHo$_2$O$_4$ yields a total moment $\boldsymbol{\mu}_{\mathbf{k}_0} = (0.0, 0.0, 6.2)\mu_B$, where the moment increases with decreasing temperature in two steps, as seen in the lower panel of Fig. 9. The inset shows the phase fraction of each irrep, normalized to 1. From $T_{N\Gamma_2} \sim 1.3$ K down to the second ordering temperature $T_{N\Gamma_1} = 0.84$ K, only Γ_2 contributes to the magnetic diffraction. At this temperature, a new set of Bragg peaks characterized by Γ_1 appears. For temperatures below the onset of the new Bragg peaks, near $T = 0.75$ K, the phase fraction stabilizes at a ratio 80% of Γ_1 and 20% of Γ_2. This conclusion is also supported by our analysis of the diffuse scattering intensity, detailed in the next section.

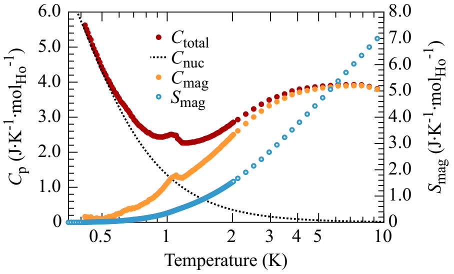

FIG. 10. Specific heat measurement of BaHo$_2$O$_4$ on single crystals as a function of T. The dark red points are the measured specific heat C_{total}, the dashed line the calculated nuclear contribution C_{nuc}, and the orange points the magnetic contribution C_{mag}, resulting from the subtraction of C_{nuc} from C_{total}. A small anomaly is located around $T = 1.2$ K, coherent with the magnetic transition observed in neutron powder diffraction. The blue circles are the magnetic entropy S_{mag}, calculated from $\int C_{\text{mag}}(T)/T\, dT$, and associated with the right-sided axis.

Previous specific heat measurements on powder of BaHo$_2$O$_4$ report only one antiferromagnetic phase transition at $T_N = 0.8$ K [23]. This is in contradiction with our own measurements on both powder and single crystal samples which show a transition at $T_N = 1.2$ K, which is close to $T_{N\Gamma_2} \sim 1.3$ K, associated with the linear extrapolation of the moment size in Fig. 9. The specific heat measurements shown in Fig. 10 were performed on small single crystals obtained through flux growth [24]. The large increase seen at the lowest temperatures is the signature of a nuclear Schottky contribution C_{nuc}. Subtracting C_{nuc} from the measured data yields the magnetic contribution C_{mag}, as, in this temperature range, the lattice contribution is negligible. The entropy S_{mag} is calculated by integrating $C_{\text{mag}}(T)/T$. While the temperature range is too narrow to show a saturation, it is interesting at this point to note that the magnetic transition has only a very small contribution to the entropy of the system. Just above $T_N = 1.2$ K, it is well below the expected value of $R\ln(2)$ for the ordering of a doublet, where R is the universal gas constant. This indicates very little difference in entropy between the fluctuating chains and long-range magnetic order.

D. 1D magnetic correlations in diffuse scattering

Diffuse scattering can be harnessed to determine useful information, not only concerning the dimensionality of the interactions, but also the size and direction of the associated moments. Furthermore, it exposes the remaining magnetism from the sites which do not order. In the following we discuss how the magnetic correlations develop along the zigzag chains in the *c* direction and how the direction of the magnetic moments—along *c* or in the *ab* plane—influences the shape of the powder spectra.

The shape of the diffuse scattering is similar to what has been observed in SrDy$_2$O$_4$ and SrHo$_2$O$_4$. The sawtooth

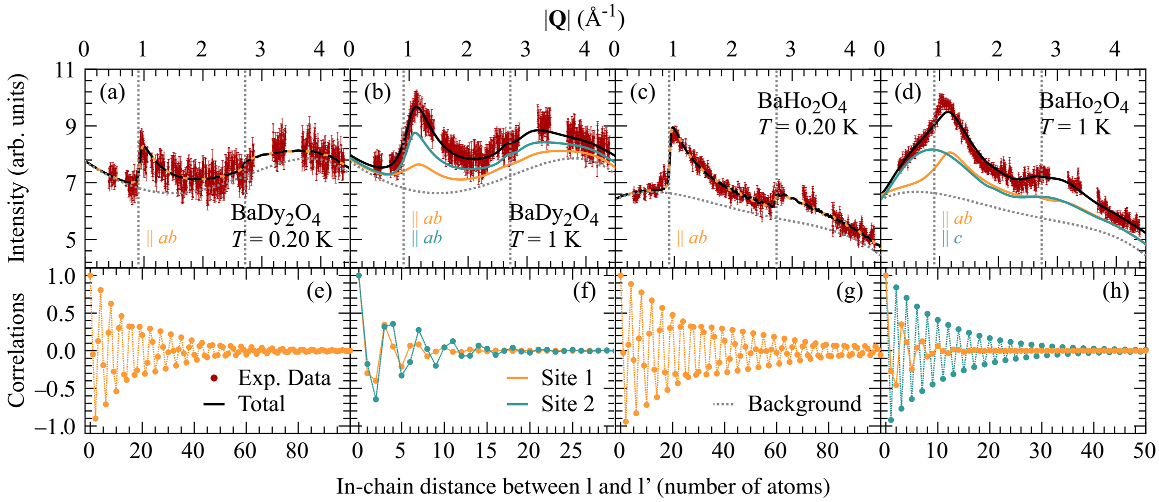

FIG. 11. Selection of diffuse scattering spectra below and above the transition temperatures for $BaDy_2O_4$ and $BaHo_2O_4$, and their fits with the ANNNI model. The red dots are the powder diffraction pattern after subtraction of the nuclear and magnetic Bragg peaks, which then consists of the diffuse magnetic signal and a background. The gaps in the experimental spectra are due to the strong nuclear peaks from the copper sample holder, which were removed. The dotted gray line is the background and the black line the total calculated scattering function, where the contribution from site 1 is shown in orange and from site 2 in blue. Panels (a) and (b) show $BaDy_2O_4$ at $T = 0.20$ K, which is below the transition, and at 1 K, which is above. A moment in the *ab* plane is present on site 1 at $T = 0.20$ K, which is kept at the same size at 1 K, where an additional moment in the same plane is added for the site 2. Panels (c) and (d) show $BaHo_2O_4$ at $T = 0.20$ K and 1 K, with a moment in the *ab* plane on site 1 and a moment along *c* on site 2. Vertical lines are placed at $|\mathbf{Q}| = \pi/c$ and $|\mathbf{Q}| = 3\pi/c$. The lower panels (e)–(h) display the correlation length between rare earth atoms within a chain as a function of the number of atoms separating them.

spectra isolated in Fig. 11 do not show the high frequency oscillations expected for the case of two- or three-dimensional correlations [8]. Therefore, it indicates that the correlations are mainly 1D. From our MULTIX calculations, we found that the moments are Ising-like, and as these sites form zigzag chains along the *c* axis, the simplest model representing these systems is the 1D ANNNI model [18]. In its original iteration, the spins are collinear in a chain with two interactions: J_1 between nearest neighbors and J_2 between next-nearest neighbors. This model is equivalent to a zigzag chain where J_1 is along the diagonal connection and J_2 along the direction of the chain, which in our case is the *c* axis.

For the analysis of the diffuse scattering, we calculated the partial differential neutron scattering crosssection per solid angle Ω, per unit energy E [34]:

$$\frac{d^2\sigma}{d\Omega\, dE_f} = \frac{|\mathbf{k}_f|}{|\mathbf{k}_i|} e^{-2W(\mathbf{Q})} \sum_{\alpha\beta} \left(\delta_{\alpha\beta} - \frac{Q_\alpha Q_\beta}{|\mathbf{Q}|^2} \right) S^{\alpha\beta}_{\mathrm{mag}}(\mathbf{Q},\omega), \tag{2}$$

which is summed over the Cartesian coordinates α and β. Here, the scattering function $S^{\alpha\beta}_{\mathrm{mag}}(\mathbf{Q},\omega)$ is defined as

$$S^{\alpha\beta}_{\mathrm{mag}}(\mathbf{Q},\omega) = \left(\frac{\gamma_n r_0 g}{2}\right) \int dt\, e^{-i\omega t} \times \sum_{ll'} f_l^*(\mathbf{Q}) f_{l'}^*(\mathbf{Q}) e^{i\mathbf{Q}\cdot(\mathbf{r}_l - \mathbf{r}_{l'})} \langle S_l^\alpha(0) S_{l'}^\beta(t)\rangle, \tag{3}$$

where $\langle S_l^\alpha(0) S_{l'}^\beta(t)\rangle$ is the spin-spin correlation function. Also, γ_n is the gyromagnetic ratio of the neutron, r_0 the classical electron radius, g the Landé g factor, $\mathbf{k}_i$ and $\mathbf{k}_f$ the wave vectors of the incident and scattered neutrons, $\mathbf{Q} = \mathbf{k}_i - \mathbf{k}_f$ the momentum transfer, $f(\mathbf{Q})$ the magnetic form factor, and $e^{-2W(\mathbf{Q})}$ the Debye-Waller factor. The sum has to be taken over all magnetic atoms. In an elastic case, where the energy transfer is negligible, a static approximation reduces the scattering function to

$$S^{\alpha\beta}_{\mathrm{mag}}(\mathbf{Q}) = \left(\frac{\gamma_n r_0 g}{2}\right) \sum_{ll'} f_l^*(\mathbf{Q}) f_{l'}^*(\mathbf{Q}) e^{i\mathbf{Q}\cdot(\mathbf{r}_l - \mathbf{r}_{l'})} \langle S_l^\alpha S_{l'}^\beta\rangle. \tag{4}$$

The spin-spin correlation function can be written as

$$\langle S_l^\alpha S_{l'}^\beta\rangle = |\boldsymbol{\mu}|^2 g_{ll'}(J_1, J_2, T), \tag{5}$$

where $g_{ll'}$ is the site dependent correlation function between the spins on positions l and l' for given interactions J_1 and J_2, at a temperature T. In the case of the 1D ANNNI model, the correlation function is known in the thermodynamic limit [35]. The powder average has to be calculated for comparison with the powder data. It is defined as the integral of the scattering function over the solid angle [36]:

$$\bar{S}(|\mathbf{Q}|) = \int \frac{d\Omega_{\hat{\mathbf{Q}}}}{4\pi} S(\mathbf{Q}). \tag{6}$$

The diffuse scattering is isolated from the diffraction pattern by subtracting the contributions from the nuclear and magnetic Bragg peaks. This results in the diffuse scattering intensity plus a background, as shown in Fig. 11. This figure shows the diffuse scattering for temperatures above and below the formation of order. Strong peaks originating from the copper sample holder were excluded from the spectra. This allows us to fit the residual spectrum using the magnetic interactions J_1 and J_2, and the moment size $|\boldsymbol{\mu}|$, as adjustable parameters. The background is fitted with a smooth fourth-order polynomial.

A closer inspection of the model shows that it is strongly dependent on the interaction ratio J_2/J_1 and is fairly insensitive to their individual values. Various combinations of J_1 and J_2, for a given interaction ratio, will produce a curve with a similar deviation χ^2 between the model and the data. Unfortunately, this means that it is not possible to determine the absolute size of J_1 and J_2, but only their ratio J_2/J_1. However, the calculated spectra are sensitive to the sign of the interaction constants, i.e., whether they are ferromagnetic or antiferromagnetic. This distinction is possible because the correlations in the ANNNI model have an incommensurate modulation at finite temperature for a wide range of ratio J_2/J_1. This modulation is temperature dependent and converges towards a commensurate value as $T \to 0$ K. Here, the commensurate value is $|\mathbf{Q}| = (\mathrm{n} + \frac{1}{2})c^* = (2\mathrm{n}+1)\pi/c$. These commensurate positions are indicated by the vertical dashed lines in Fig. 11. Sharp features in the diffuse scattering are located near these values and reflect the incommensurate modulation of the correlations. The sign of J_1 determines if the incommensurate value is larger or smaller than the zero-temperature commensurate value. Consequently, this determines if the leading edge of these sawtooth features is to the left or the right of the dashed line in Fig. 11. For a negative J_1, the edge is located on the right. That the periodicity is inversely proportional to c is a further indication of the 1D character of these interactions.

Furthermore, the fact that neutrons interact only with magnetic moments which are perpendicular to the momentum transfer strongly affects the profile of the diffuse scattering. The dot product $\mathbf{Q} \cdot (\mathbf{r}_l - \mathbf{r}_{l'})$ in $S^{\alpha\beta}_{\mathrm{mag}}(\mathbf{Q}, \omega)$ results in a much stronger contribution for any $\mathbf{Q}$ along the rare earth chains, which run parallel to the c axis. A spin orientation along c produces a significantly lower scattering intensity with broader features than a spin in the ab plane. This is the reason why a spin along c can be hard to detect in the presence of a large spin component residing in the ab plane. The geometry of the chains also makes it hard to distinguish an alignment of the spins along a or b.

The model contains one zigzag chain. In our structure, the two crystallographically inequivalent rare earth atoms are interacting along separated chains, resulting in a total of four chains within a chemical unit cell: two on site 1, two on site 2. As the two types of chain are sitting on two inequivalent sites, they are treated with their own set of magnetic interactions J_1 and J_2, and moment $\boldsymbol{\mu}$. The only difference between the chains A and B of a given rare earth site will be the atomic position, as shown in Fig. 8. The total calculated spectra will then consist of the sum of the contributions from these four chains, plus a background. The number of atoms contained in a chain is set to such a high number that the correlations converge to zero over the length of the chain.

While the model includes size and direction of the moments, only the sizes are fitted, with the directions fixed to the easy axis obtained from the CEF calculations. The contributions from each site are shown as the orange and blue curves in Fig. 11. In order to keep the size of the moments stable, the polynomial background was fitted at a temperature where there is a clear and known contribution from both sites. The background was kept fixed afterwards. The size of the moments is determined by scaling the moment in Eq. (5) such that the difference between the higher and lower plateaus of the temperature dependent scattering function corresponds to the size of the moments as determined from the FULLPROF refinements. The results of this procedure are presented in Fig. 12.

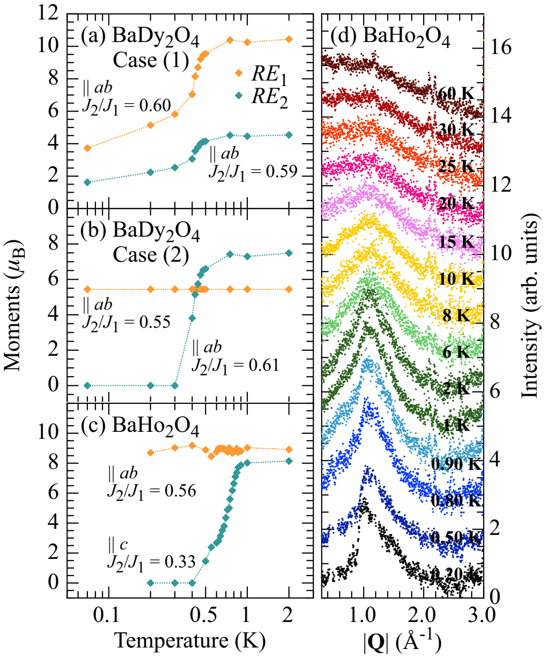

FIG. 12. Parameters from fitting the diffuse magnetic scattering with the 1D ANNNI model. The intensities associated with the different sites are scaled with respect to the total ordered moment in each compound. Panel (a) shows case (1) for BaDy$_2$O$_4$, where we assumed that both sites order but also remain in a fluctuating state. Panel (b) is the case (2) where the remaining diffuse scattering is assigned to a single site which does not order and has a fixed moment. The other site then sees a strong decrease in the size of the moment with the onset of magnetic order. Panel (c) shows for BaHo$_2$O$_4$ the decreasing size of the moment of site 2. The moment on site 1, which remains in a strongly fluctuating state, is temperature independent. Panel (d) presents a waterfall plot showing the complete evolution of an isolated region of diffuse scattering of BaHo$_2$O$_4$ from $T = 0.20$ K to 60 K. The correlations are still clearly visible at $T = 60$ K.

Since the systems do not show significant structural change with temperature, the ratio of the exchange constants are therefore expected to remain constant. This temperature independent ratio was obtained while simultaneously fitting several spectra recorded at a number of temperatures. This strategy was chosen to alleviate problems which could skew this value if too many spectra at temperatures close to the phase transition were chosen. Spectra taken at the lowest measured temperatures are also discarded, as different chains will eventually start to interact with each other. This fitting procedure provides a complete description of the shape and position of the sawtooth features as a function of temperature for both BaDy$_2$O$_4$ and BaHo$_2$O$_4$, giving compelling evidence to the proposed model. However, we cannot disregard completely that other types of short-range correlations could reproduce our data. Measurements on single crystals are required for a definitive description of these systems.

1. $BaDy_2O_4$

The sharp sawtooth seen at $T = 1$ K in $BaDy_2O_4$ suggests that only magnetism in the *ab* plane is present, with no contribution from moments parallel to the *c* axis, as this would result in broader features. This is also coherent with the direction of the moments obtained from MULTIX. The ANNNI model was fitted with moments in the *ab* plane for both sites. The experimental scattering intensity in Figs. 11(a) and 11(b) strongly decreases with temperature, but stabilizes at $T = 0.30$ K. It is interesting to note that the diffuse scattering intensity persists down to $T = 0.07$ K, after the onset of magnetic Bragg peaks. The diffusive intensity at $T = 0.07$ K has only dropped to half of the intensity at $T = 1$ K. As expected, the trend for the magnetic scattering intensity is the opposite to that of the one seen for the magnetic Bragg peaks: the intensity of the diffuse magnetic scattering decreases with lower temperatures. This seems to indicate that weight from the diffusive scattering is transferred to the magnetic Bragg peaks.

This leads to two possible scenarios, presented in Figs. 12(a) and 12(b). In scenario (1) the magnetic moments, which are responsible for the diffuse scattering, are on both sites, and have the same temperature dependence, as seen in the thermal evolution of the magnetic Bragg peaks. However, this would mean that despite the magnetic order manifested through the presence of Bragg peaks, moments of the size of nearly $4\mu_B$ and $2\mu_B$ would continue to fluctuate down to $T = 0.07$ K. Scenario (2) is the case where one of the sites is not ordering. Here, the intensity of the diffuse scattering associated with site 2, which does order, decreases to zero at the lowest temperatures. The diffuse scattering seen at low temperature will then be entirely located on site 1 with a moment of the size of $5.2(2)\mu_B$. This is the scenario shown in Figs. 11(a) and 11(b).

For case (1), shown in Fig. 12(a), both sites have antiferromagnetic interactions with their nearest neighbors and next-nearest neighbors. The ratios J_2/J_1 are 0.59 and 0.60 for sites 1 and 2, respectively, which are both higher than 1/2. This implies that the atoms in the chains of both sites are interacting as a double Néel state, consistent with the FULLPROF analysis.

For case (2), shown in Fig. 12(b), similar values are obtained with J_2/J_1 of 0.55 and 0.61 for sites 1 and 2, respectively. As expected, the site that does not order has a ratio J_2/J_1 which is closer to the critical value of 1/2. For this case, the moment on site 1 was fitted at low temperatures.

The correlation function, which gives the distance over which sites are correlated, is shown in the lower panels of Fig. 11. Temperature and the ratio J_2/J_1 are affecting this length: it decreases with increasing temperature, or for a J_2/J_1 ratio closer to 1/2. This is consistent with the observation that the sites that eventually order have a larger ratio of J_2/J_1 than the fluctuating sites. For case (1), where both sites remain in a fluctuating state, both will have an interaction range of about 20 neighbors at $T = 1$ K, which increases to nearly 150 neighbors at 0.20 K. For case (2), where one site does not order, the correlation range is shorter at $T = 1$ K, with 10 neighbors, and it increases to 100 neighbors at 0.20 K.

Given that the two magnetic orders possess two different propagation vectors, it is likely that the two orders develop on a different sites. This was the interpretation resulting from the magnetic Bragg peaks refinement. Case (1) would then be the correct one. Unfortunately, we are unable to give a definitive answer from our analysis of the powder spectra.

2. $BaHo_2O_4$

For $BaHo_2O_4$, the analysis of the diffuse scattering at $T = 1$ K is shown in Fig. 11(d). The shape of the spectra indicates the presence of magnetic moments in the *ab* plane, as well as along the *c* axis. The component along *c*, placed on site 2, decreases in intensity with temperature, as expected due to the magnetic order that develops with moments in that direction. The intensity of the moment in the *ab* plane on site 1 remains constant in the temperature range from 2 to 0.20 K, as shown in Fig. 12(c). This result suggests that site 1 does not order down to 0.20 K and remains in a strongly fluctuating state. From our analysis, we can thus conclude that the moment on site 1 lies in the *ab* plane with a moment size of $8.8(3)\mu_B$, which is consistent with the MULTIX calculations. This is another indication of the fact that the magnetic orders of both irreps coexist on site 2. The result of this fit is shown in Fig. 12(c), where the size of the moment on site 1 remains constant, and the one on site 2 decreases to zero. Here, one can clearly see the different transition temperatures of the two irreps on site 2. The moment slightly decreases between $T = 2$ and 0.80 K, as the order associated with $\mathbf{k}_{\Gamma_2}$ develops but then drops sharply once the order associated with $\mathbf{k}_{\Gamma_1}$ sets in.

Site 1, which does not order, is characterized by all antiferromagnetic interactions with a ratio $J_2/J_1 = 0.56$, similar to $BaDy_2O_4$'s double Néel states. Site 2, which orders, has a much lower ratio of 0.33—below the critical value of 1/2—again with all antiferromagnetic interactions. It describes a simple Néel order, consistent with the FULLPROF analysis. The site that does not order also has a J_2/J_1 which is much closer to the critical value of 1/2. At $T = 1$ K, site 2 has correlations with up to 50 neighbors, while site 1 will interact with only 15 neighbors. At 0.20 K, the correlation length of site 1 increases to more than 150 sites.

The fits were limited to temperatures below 2 K, but for $BaHo_2O_4$ multiple spectra were recorded at temperatures above 2 K which show strong diffuse scattering and sharp features up to 60 K, as can be seen in Fig. 12(d). However, the ANNNI model with fixed J_1 and J_2 is unable to describe the observed spectra for the higher temperatures. A good fit would require unphysically large magnetic moment sizes, or a significant change in the values of J_1 and J_2, which is not expected, as there is no significant change in the crystal structure. On the other hand, higher CEF levels start to mix in at higher temperatures, as our MULTIX calculations show these to be close in energy.

Nonetheless, the quality of the fits at lower temperature is an indication for the presence of strong 1D correlations in these systems, as was observed in the case of $SrDy_2O_4$ and $SrHo_2O_4$ [8]. While additional interactions J_3 and J_4 between the chains, as defined in Fig. 8, are expected to be non-negligible at very low temperatures [7], the ANNNI model still adequately accounts for the diffusive part of our spectra.

III. DISCUSSION AND CONCLUSION

In conclusion, we have performed CEF calculations using MULTIX to interpret our inelastic neutron scattering spectra. From these, we find a site-dependent magnetic anisotropy as well as the presence of an easy axis, which is confined to either the *ab*-plane or along the *c* axis. We measured the temperature dependence of the neutron powder diffraction signal which we used to perform a refinement of the magnetic Bragg peaks. These spectra show strong diffusive components, which we fitted using a 1D ANNNI model, confirming the coexistence of long-range and short-range magnetic order in both samples. In $BaDy_2O_4$, we observe magnetic order with two different wave vectors but a single transition temperature of $T_N = 0.48$ K. The ordered moments are restricted to the *ab* plane. Magnetic fluctuations remain important to the lowest temperatures, even after the ordered moments saturate. The direction of the fluctuating moments are shown to be in the *ab* plane, the same plane as the long-range order. For $BaHo_2O_4$, the magnetic order has to two different irreps with the same propagation vector $\mathbf{k}_0 = (0,0,0)$. The transitions occur at different temperatures, one at $T_{N\Gamma_1} = 0.84$ K and the other at $T_{N\Gamma_2} \sim 1.3$ K. For both, the moments order along the *c* axis. Magnetic fluctuations also remain after the order saturates, predominantly in the *ab* plane. Agreements between the intensities of the modeled diffuse scattering and of the Bragg peaks indicate that interactions in these samples are for the most part 1D and confined within a specific zigzag chain.

This shares similarities with the behavior seen in $Sr(Dy,Ho)_2O_4$. In $SrHo_2O_4$, sites 1 and 2 are hosts of a simple Néel long-range order along the *c* axis, and a double Néel short-range order in the *ab* plane, respectively [7]. On the other hand, no long-range order has been found in $SrDy_2O_4$, but a detailed analysis of the diffuse scattering shows the presence of short-range correlations on both sites, with a spin alignment nonetheless in the same directions as the sites of $SrHo_2O_4$[10].

The compounds $SrHo_2O_4$ [3,5–8], $SrEr_2O_4$ [2,4], and $BaNd_2O_4$ [37], either through powders or single crystals neutron diffraction, show the coexistence of long-range (or quasi-long-range) order and short-range order. So far, however, $SrYb_2O_4$ [12] is the only system where two long-range orders were reported. Other compounds such as $BaTb_2O_4$ [38] and $SrDy_2O_4$ [8] are only exhibiting short-range order, while $BaTm_2O_4$ [9] does not show any sign of ordering. Of all the compounds studied in this family, only $SrGd_2O_4$ shows two separated magnetic transition temperatures in zero field, as seen from specific heat measurements [39]. Its magnetic structure still remains unsolved. Another compound which stands out is $SrTb_2O_4$ [40], where the long-range order is incommensurate.

With our results on $BaDy_2O_4$ and $BaHo_2O_4$, we confirm the presence of two different types of long-range magnetic order—with different transition temperatures in one case—coexisting with fluctuating moments down to the lowest measured temperatures, unveiling two compounds with interesting and complex magnetic interactions. Measurement on single crystals will soon follow. This will allow us to describe more precisely the evolution of the diffuse scattering, especially with the use of polarized neutron scattering measurements which will help to separate the contributions from the different sites. This would also allow us to study the formation of magnetic domains which were seen in $Sr(Dy,Ho)_2O_4$ [7,10].

A conservative scenario for both samples is that only one of the sites orders—hosting two types of magnetic order—and the other one remains fluctuating down to the lowest measured temperatures. However, from a combination of CEF calculations, refinement of the Bragg peaks, and a description of the nature of the diffuse scattering, there are strong indications for more exotic magnetic behaviors. In the case of $BaDy_2O_4$, we suggest the interesting possibility that both sites order, but keep fluctuating down to the lowest temperatures. This could then be a case of magnetic fragmentation, which as been observed in the spin liquid phase of a pyrochlore, where magnetic order and fluctuations coexist on the same site [41,42]. Indications for a *classical* spin liquid ground state was indeed found from an investigation by ultrasound velocity measurements in the related compound $SrDy_2O_4$ [14], as well as by muon spin relaxation measurements [43]. $BaDy_2O_4$ might presents a new class of magnetic ground state whose nature is yet to be determined, which surely present an interesting challenge.

Concerning $BaHo_2O_4$, we propose a scenario in which only one of the two magnetic sites is ordering, initially at $T_{N\Gamma_2} \sim 1.3$ K. A second order on the same site, with a different irrep, takes place at $T_{N\Gamma_1} = 0.84$ K, leading to a separation of the magnetic phase. The two phase fractions evolve until they reach proportions of 20%–80%, where the fraction associated with Γ_1 becomes dominant. This scenario might be the result of the growing influence of the interchain interactions as the temperature is lowered. These interactions are required for long-range order, and their evolving influence could suddenly privilege one order over the other.

ACKNOWLEDGMENTS

The research at the Université de Montréal received support from the Natural Sciences and Engineering Research Council of Canada (NSERC), the Fonds de Recherche du Québec Nature et Technologies (FRQNT), and the Canada Research Chair Foundation, and the work at PSI received support from the Swiss National Foundation (SNF Grant No. 138018).

---

[1] H. Karunadasa, Q. Huang, B. G. Ueland, J. W. Lynn, P. Schiffer, K. A. Regan, and R. J. Cava, Phys. Rev. B **71**, 144414 (2005).

[2] O. A. Petrenko, G. Balakrishnan, N. R. Wilson, S. de Brion, E. Suard, and L. C. Chapon, Phys. Rev. B **78**, 184410 (2008).

[3] S. Ghosh, H. D. Zhou, L. Balicas, S. Hill, J. S. Gardner, Y. Qiu, and C. R. Wiebe, J. Phys.: Condens. Matter **23**, 164203 (2011).

[4] T. J. Hayes, G. Balakrishnan, P. P. Deen, P. Manuel, L. C. Chapon, and O. A. Petrenko, Phys. Rev. B **84**, 174435 (2011).

[5] O. Young, L. C. Chapon, and O. A. Petrenko, J. Phys. Conf. Ser. **391**, 012081 (2012).

[6] O. Young, A. R. Wildes, P. Manuel, B. Ouladdiaf, D. D. Khalyavin, G. Balakrishnan, and O. A. Petrenko, Phys. Rev. B **88**, 024411 (2013).

[7] J. J. Wen, W. Tian, V. O. Garlea, S. M. Koohpayeh, T. M. McQueen, H.-F. Li, J. Q. Yan, J. A. Rodriguez-Rivera, D. Vaknin, and C. L. Broholm, Phys. Rev. B **91**, 054424 (2015).

[8] A. Fennell, V. Y. Pomjakushin, A. Uldry, B. Delley, B. Prévost, A. Désilets-Benoit, A. D. Bianchi, R. I. Bewley, B. R. Hansen, T. Klimczuk, R. J. Cava, and M. Kenzelmann, Phys. Rev. B **89**, 224511 (2014).

[9] H.-F. Li, A. Senyshyn, O. Fabelo, J. Persson, B. Hou, M. Boehm, K. Schmalzl, W. Schmidt, J.-P. Vassalli, P. Thakuria, X. Sun, L. Wang, G. Khazaradze, B. Schmitz, C. Zhang, G. Roth, J. G. Roca, and A. Wildes, J. Mater. Chem. C **3**, 7658 (2015).

[10] N. Gauthier, A. Fennell, B. Prévost, A.-C. Uldry, B. Delley, R. Sibille, A. Désilets-Benoit, H. A. Dabkowska, G. J. Nilsen, L.-P. Regnault, J. S. White, C. Niedermayer, V. Pomjakushin, A. D. Bianchi, and M. Kenzelmann, Phys. Rev. B **95**, 134430 (2017).

[11] T. J. Hayes, O. Young, G. Balakrishnan, and O. A. Petrenko, J. Phys. Soc. Jpn. **81**, 024708 (2012).

[12] D. L. Quintero-Castro, B. Lake, M. Reehuis, A. Niazi, H. Ryll, A. T. M. N. Islam, T. Fennell, S. A. J. Kimber, B. Klemke, J. Ollivier, V. G. Sakai, P. P. Deen, and H. Mutka, Phys. Rev. B **86**, 064203 (2012).

[13] T. H. Cheffings, M. R. Lees, G. Balakrishnan, and O. A. Petrenko, J. Phys.: Condens. Matter **25**, 256001 (2013).

[14] C. Bidaud, O. Simard, G. Quirion, B. Prévost, S. Daneau, A. D. Bianchi, H. A. Dabkowska, and J. A. Quilliam, Phys. Rev. B **93**, 060404 (2016).

[15] O. A. Petrenko, O. Young, D. Brunt, G. Balakrishnan, P. Manuel, D. D. Khalyavin, and C. Ritter, Phys. Rev. B **95**, 104442 (2017).

[16] N. Gauthier, A. Fennell, B. Prévost, A. Désilets-Benoit, H. A. Dabkowska, O. Zaharko, M. Frontzek, R. Sibille, A. D. Bianchi, and M. Kenzelmann, Phys. Rev. B **95**, 184436 (2017).

[17] T. Fennell, M. Kenzelmann, B. Roessli, H. Mutka *et al.*, Phys. Rev. Lett. **112**, 017203 (2014).

[18] W. Selke, Phys. Rep. **170**, 213 (1988).

[19] F. Heidrich-Meisner, I. A. Sergienko, A. E. Feiguin, and E. R. Dagotto, Phys. Rev. B **75**, 064413 (2007).

[20] H.-J. Mikeska and A. K. Kolezhuk, *Quantum Magnetism*, edited by U. Schollwöck, J. Richter, D. J. J. Farnell, and R. F. Bishop, Lecture Notes in Physics Vol. 645 (Springer, Berlin, 2004).

[21] I. P. McCulloch, R. Kube, M. Kurz, A. Kleine, U. Schollwöck, and A. K. Kolezhuk, Phys. Rev. B **77**, 094404 (2008).

[22] K. Okunishi and T. Tonegawa, Phys. Rev. B **68**, 224422 (2003).

[23] Y. Doi, W. Nakamori, and Y. Hinatsu, J. Phys.: Condens. Matter **18**, 333 (2006).

[24] T. Besara, M. S. Lundberg, J. Sun, D. Ramirez, L. Dong, J. B. Whalen, R. Vasquez, F. Herrera, J. R. Allen, M. W. Davidson, and T. Siegrist, Prog. Solid State Chem. **42**, 23 (2014).

[25] R. I. Bewley, R. S. Eccleston, K. A. McEwen, S. M. Hayden, M. T. Dove, S. M. Bennington, J. R. Treadgold, and R. L. S. Coleman, Physica B **385-386**, 1029 (2006).

[26] D. Schmitt and B. Ouladdiaf, J. Appl. Crystallogr. **31**, 620 (1998).

[27] A. Uldry, F. Vernay, and B. Delley, Phys. Rev. B **85**, 125133 (2012).

[28] P. Fischer, G. Frey, M. Koch, M. Könnecke, V. Pomjakushin, J. Schefer, R. Thut, N. Schlumpf, R. Bürge, U. Greuter, S. Bondt, and E. Berruyer, Physica B **276-278**, 146 (2000).

[29] J. Rodríguez-Carvajal, Physica B **192**, 55 (1993).

[30] M. P. Marder, *Condensed Matter Physics* (John Wiley & Sons, New York, 2010).

[31] B. Z. Malkin, S. I. Nikitin, I. E. Mumdzhi, D. G. Zverev, R. V. Yusupov, I. F. Gilmutdinov, R. Batulin, B. F. Gabbasov, A. G. Kiiamov, D. T. Adroja, O. Young, and O. A. Petrenko, Phys. Rev. B **92**, 094415 (2015).

[32] B. E. Warren, Phys. Rev. **59**, 693 (1941).

[33] R. C. Jones, Acta Crystallogr. **2**, 252 (1949).

[34] Z. Yamani, Z. Tun, and D. H. Ryan, Can. J. Phys. **88**, 771 (2010).

[35] J. Stephenson, Can. J. Phys. **48**, 1724 (1970).

[36] J. T. Haraldsen, T. Barnes, and J. L. Musfeldt, Phys. Rev. B **71**, 064403 (2005).

[37] A. A. Aczel, L. Li, V. O. Garlea, J. Q. Yan, F. Weickert, M. Jaime, B. Maiorov, R. Movshovich, L. Civale, V. Keppens, and D. Mandrus, Phys. Rev. B **90**, 134403 (2014).

[38] A. A. Aczel, L. Li, V. O. Garlea, J. Q. Yan, F. Weickert, V. S. Zapf, R. Movshovich, M. Jaime, P. J. Baker, V. Keppens, and D. Mandrus, Phys. Rev. B **92**, 041110 (2015).

[39] O. Young, G. Balakrishnan, M. R. Lees, and O. A. Petrenko, Phys. Rev. B **90**, 094421 (2014).

[40] H.-F. Li, C. Zhang, A. Senyshyn, A. Wildes, K. Schmalzl, W. Schmidt, M. Boehm, E. Ressouche, B. Hou, P. Meuffels, G. Roth, and T. Brückel, Front. Phys. **2**, 42 (2014).

[41] M. E. Brooks-Bartlett, S. T. Banks, L. D. C. Jaubert, A. Harman-Clarke, and P. C. W. Holdsworth, Phys. Rev. X **4**, 011007 (2014).

[42] S. Petit, E. Lhotel, B. Canals, M. C. Hatnean, J. Ollivier, H. Mutka, E. Ressouche, A. R. Wildes, M. R. Lees, and G. Balakrishnan, Nat. Phys. **12**, 746 (2016).

[43] N. Gauthier, B. Prévost, A. Amato, C. Baines, V. Pomjakushin, A. D. Bianchi, R. J. Cava, and M. Kenzelmann, J. Phys. Conf. Series **828**, 012014 (2017).